American Society of Mechanical Engineers

ASME Accepted Manuscript Repository

Institutional Repository Cover Sheet

Cranfield Collection of E-Research - CERES

ASME Paper Title: Aeroelastic analysis of a single element composite wing in ground effect using Fluid Structure Interaction

Authors: Chris Sungkyun Bang, Zeeshan Rana, László Könözsy, Veronica M. Rodriguez, Clive Temple

ASME Journal Title: Journal of Fluids Engineering

Volume/Issue: Volume 144, Issue 4, 041202 Date of Publication (VOR* Online) 20 November 2021

ASME Digital Collection URL: https://asmedigitalcollection.asme.org/fluidsengineering/article/doi/10.1115/1.4053089/1128810/Aeroelastic-Analysis-of-a-Single-Element-Composite

DOI: https://doi.org/10.1115/1.4053089

*VOR (version of record)

Journal of Fluids Engineering
Volume 144, Issue 4, April 2022, Article number 041202, Paper number FE-21-1108

Aeroelastic analysis of a single element composite wing in ground effect using Fluid Structure Interaction

Chris Sungkyun Bang
Cranfield University
Cranfield University, College Road, Cranfield, Bedfordshire, UK, MK43 0AL
s.bang@cranfield.ac.uk

Zeeshan A. Rana
Cranfield University
Cranfield University, College Road, Cranfield, Bedfordshire, UK, MK43 0AL
zeeshan.rana@cranfield.ac.uk

László Könözsy
Cranfield University
Cranfield University, College Road, Cranfield, Bedfordshire, UK, MK43 0AL
laszlo.konozsy@cranfield.ac.uk

Veronica Marchante Rodriguez
Cranfield University
Cranfield University, College Road, Cranfield, Bedfordshire, UK, MK43 0AL
v.marchanterodriguez@cranfield.ac.uk

Clive Temple
Cranfield University
Cranfield University, College Road, Cranfield, Bedfordshire, UK, MK43 0AL
C.Temple@cranfield.ac.uk

ABSTRACT

The present work focuses on an advanced coupling of computational fluid dynamics (CFD) and structural analysis (FEA) on the aeroelastic behaviour of a single element inverted composite wing with the novelty of including the ground effect. The front wing of the Formula One (F1) car can become flexible under the fluid loading due to elastic characteristics of composite materials, resulting in changing the flow field and eventually altering overall aerodynamics. The purpose of this study is to setup an accurate fluid-structure interaction (FSI) modelling framework and to assess the influence of elastic behaviour of the wing in ground effect on the aerodynamic and structural performance. Different turbulence models are studied to better capture the changes of the flow field and variation of ride heights are considered to investigate the influence of ground effect on aerodynamic phenomena. A steady-state two-way coupling method is exploited to run the FSI numerical simulations using ANSYS, which enables simultaneous calculation by coupling CFD with FEA. The effect of various composite structures on the wing performance is extensively studied concerning structure configuration, ply orientation and core materials. The numerical results generally represent good agreement with the experimental data, however, discrepancy, especially in the aerodynamic force, is presented. This may be consequence of less effective angle of attack due to the wing deflection and deterioration of vortex-induced effect. For the structural analysis, the woven structure gives rise to more stable structural deflection than the unidirectional structure despite the associated weight penalty.

Published by The American Society of Mechanical Engineers. This is the Author Accepted Manuscript issued with: Creative Commons Attribution License (CC BY).
The final published version is available online at DOI:10.1115/1.4053089.Please refer to any applicable publisher terms of use.

Keyword: fluid-structure interaction (FSI), aeroelasticity, ground effect, composite structure, Two-way coupling, structural deformation

1. INTRODUCTION

Among aerodynamic components to affect performance of Formula One (F1) racing cars, the front wing operated in ground proximity contributes approximately 30% of total downforce [1], which is used in line with mechanical grip to improve acceleration, braking, and cornering speed. In addition to the front wing's aero performance, the wing, as the first component directly interacting with fresh airflow, plays an important role in controlling the airflow which interacts with downstream features such as undertray or rear wing, thus ensuring they contain high-energy flow with low turbulence intensities. Figure 1 shows a typical Formula One car with an inverted front wing.



Figure 1 A Formula One car with an inverted front wing [2]

During the 2011 Australian Grand Prix it was apparent that, Red Bull RB6's flexi-wing design enabled the tips of the front wing to bend far closer to the ground compared to those of their rivals [3]. Observation showed that the wing was deflected under fluid loading with the resultant of aerodynamic benefits. Although the relevant technical regulation stipulated that aerodynamic components, including the front wing, should be

regarded as rigid bodies and must comply with the load and deflection test, F1 engineers exploited the phenomenon of 'Aero Elasticity' to improve the aerodynamic performance. In essence they circumvented the regulation governing the bodywork of the F1 car, mainly its wings, to facilitate flexing, which alters the flow characteristics and the shape of vortex structure, lowering the ground clearance.

Many studies have been conducted to investigate the inverted wing aerodynamics in ground effect by means of experimentation and computation. The first computational investigation into this was started by Katz [4–6] in which a single-element wing in ground effect was modelled and investigated using a panel method. As a consequence of a lack of viscous effect in his study, downforce reduction was not represented at low ride height. A single element GA(W)-1 wing was investigated at various ride heights from out of the ground effect up to ground proximity experimentally and computationally [7]. It was observed that the downforce increased as the ground was approached. However, when comparing this with numerical results gained using a two-dimensional panel method, there was a huge discrepancy of force measurement at lower heights. Ranzenbach and Barlow [8–11] presented experimental results of two-dimensional aerofoils in ground effect in a fixed ground wind tunnel in comparison with computation results using a Reynolds-Averaged Navier-Stokes (RANS) solver. A single element aerofoil was tested at different ride heights with a fixed angle of attack. It was found that the downforce sharply dropped below ground clearance of 0.1c. This was defined as the force reduction phenomenon due to merging of the wing and ground boundary layers. The computational solution presented this phenomenon as well.

However, the results obtained from a moving ground wind tunnel produced a greater magnitude of downforce and higher ride height at which the force reduction phenomenon occurs. An extensive investigation into wing in ground effect was performed in a moving ground wind tunnel by Zerihan and Zhang [12–15]. This faciliteated further investigation of the ground effect. Their experiments showed the results of surface pressure, overall forces and wake flow using laser Doppler anemometry (LDA) and particle image velocimetry (PIV) methods. The computation results were produced using a RANS solver modelled by the Spalart-Allmaras model [16] and the k-ω SST model [17], and showed good qualitive trends for the aerodynamic performance regarding surface pressures and wake thickness when compared with the experimental data [15]. In another study, Lawson et al. [18] carried out a computational study of a GA(W)-1 aerofoil in ground effect using RANS equations modelled by the Spalart-Allmaras model [16]. Comparing the numerical results with the experimental data obtained by PIV method, significant discrepancy was observed due to the application of different freestream velocities in each study. The pressure and wake of an inverted cambered aerofoil in ground effect was numerically investigated by Mahon and Zhang [19] by solving RANS equations. The simulations were found to offer reasonable trends of flow field regarding surface pressure distribution, sectional forces, and wake profile at various ride heights in comparison with the experimental data. Recently, numerical studies on the wing performance were carried out. Arrondeau and Rana [20] performed computational analysis on a multi-element wing with implementation of the humpback whale flipper to improve the aerodynamic efficiency. Castro and Rana [21]

also investigated the multi-element wing performance in terms of structural configuration modelled with different materials. In both studies, the wing was considered as a rigid body and elasticity was not taken into account. Although the inverted wing in ground effect has been thoroughly investigated experimentally and computationally. These studies are restricted to the flow characteristics such as forces, surface pressure and wake flow. Additionally, to the best of our knowledge, the numerical simulations are performed assuming the wing to be a rigid body. This is problematic as it is not how the wing works in reality.

Due to the fact that the aero-structural interaction is too complicated to obtain, analytical equations and experiments are limited in scope owing to its strong nonlinearity and multidisciplinary nature, a numerical approach known as fluid-structure interaction (FSI) may be employed. In addition, with recent advances in computer technology, an efficient numerical algorithm can be exploited to resolve sophisticated FSI engineering problems. The computational solution using FSI analysis plays an important role in many scientific and engineering sectors such as aerospace, wind engineering, automotive, and hydrodynamics. In aerospace engineering, aeroelasticity is one of the key factors to be considered in design process to avoid aeroelastic problems such as divergence or flutter [22–24]. Accurate FSI modelling of wind turbine blades is crucial in the development of large wind turbines which are more susceptible to aeroelastic response [25–27]. Large blades under aerodynamic loading can cause additional vibration that could result in unbalanced load alteration and instability

problems so that ultimately it could have a significant impact on the whole wind turbine system.

In the automotive sector, research has been undertaken related to aeroelastic behaviour of car components. Gayland et al. [28] simulated the interaction of transient flow fields with the structure of a vehicle hood using a one-way coupling, continuing the development of a methodology that can be utilised early in the design phase of a vehicle to capture and resolve potential panel vibration issues. Ratzel and Dias [29] studied a generic car model with a flexible/deformable flap at the rear end using a coupled transient FSI simulation. Several shape variations of the flap causing reduction in the maximum deflection are identified and used in an optimisation loop to determine a flap design with minimum displacement. Similarly, Patil et al. [30] used a two-way weakly coupled method to simulate an FSI model of a chin spoiler around the airflow. The local and global flow field changes due to the interaction between them and its effect on vehicle drag was discussed. The numerical results were validated by experiments carried out in a wind tunnel. Andreassi et al. [31] presented an example of FSI approach in the study of a Formula One car front wing with different speed and angle of attack. However, the ground effect was not applied as the bottom was stationary. One of the recent works published regarding FSI analysis in automotive application is to investigate hydroplaning phenomenon between a tyre and water road surfaces by incorporating finite element methods and Navier-Stokes equations [32]. It was found that a FSI model combined with two commercial packages shows better agreement with empirical model despite more computational resources.

Several studies used the FSI approach to investigate performance of a hydrofoil used for hydraulic machinery system [33,34]. It was demonstrated that the FSI model connected with two-way coupling method is proved to be appropriate for accurately predicting the effect of added mass and hydrodynamic damping ratio on its performance. Furthermore, Smith et al [35] studied the cavitation behaviour of the flow field caused by the effect of FSI and Dincer et al [36] suggested a new FSI monolithic approach to solve fluid-structure coupled problems simultaneously.

Evidence suggests that in racing application, investigation into the inverted wing in ground effect has been extensively studied experimentally and computationally due to its substantial benefit to performance. However, it seems that there have been few comparative studies carried out to predict accurate inverted wing performance considering aeroelastic response using advanced computational methodology. This work aims to investigate the influence of aeroelastic behaviour of a single element inverted wing including the ground effect on the aerodynamic performance using a two-way coupled FSI method by joining of CFD with FEA solutions. Computational analysis on the FSI inverted wing is performed to indicate the flow characteristics in terms of surface pressure distribution, aerodynamic forces, and wake profile. A number of ride heights are studied describing variation of the force regions. In addition to the aerodynamic performance analysis, the effect of structural characteristics with various combination of composite structure on the performance is also studied.

2. RESEARCH DESCRIPTION

2.1 Numerical modelling framework

Fluid-structure interaction (FSI) is defined as the mutual interaction between a deformable structure and an internal or surrounding fluid flow [37]. The fundamental consideration when developing a numerical simulation algorithm is the choice of appropriate governing equations of the continuum, which determines relationship between the deforming structure and fluid domain and ability of numerical method to deal with large distortions [38]. Based on the design type of scientific and engineering systems where fluid-structure interaction is concerned, different approaches of numerical procedure may be employed. One of possible methods to solve these multi-physics problems may be categorized into two approaches: the monolithic approach and the partitioned approach. The monolithic approach containing governing equations for the fluid and structure dynamics within a single mathematical framework is solved simultaneously with a solitary solver [39,40]. This approach can produce better accuracy for multidisciplinary problems; however, it may require significant effort to develop a code for a particular combination of such problems. On the contrary, the partitioned approach including governing equations of the fluid and structure dynamics is solved separately with two individual solvers [41]. This approach enables to reduce time for code development by integrating existing available codes or numerical algorithms, which have been proved and used for sophisticated FSI problems. The focus, however, should lie in correlating the fluid and structure algorithms in order to achieve stability of

the coupling method. As shown in [38], the coupled FSI model can be represented by Eq. (1).

$$\begin{bmatrix} M_s & 0 \\ \rho_0 R^T & M_f \end{bmatrix} \begin{Bmatrix} \ddot{U} \\ \ddot{P} \end{Bmatrix} + \begin{bmatrix} K_s & -R \\ 0 & K_f \end{bmatrix} \begin{Bmatrix} U \\ P \end{Bmatrix} = \begin{Bmatrix} F_S \\ F_f \end{Bmatrix} \quad (1)$$

Where M_s and K_s are the structural mass matrix and structural stiffness matrix and U, $\ddot{U}$, F_s are the nodal displacement, the second derivative of nodal displacement and the structural load vector, respectively. In the same manner, M_f and K_f are the fluid mass matric and the fluid stiffness matrix, and P, F_f, $\ddot{P}$ are the nodal pressure, the second derivative nodal pressure and the fluid load vector, respectively. R is a coupling matrix of the fluid structure interaction interface.

The fluid exerts pressure loads on the structure, causing it to deform, at the same time, the fluid geometric domain is updated considering the structural deformations. In the partitioned approach, the information gained from each numerical algorithm is shared at the boundary between them, the fluid structure interface, which is dependent on one-way or two-way coupling methods as shown in Figure 2. In one-way coupling, the calculated fluid forces from CFD analysis is transferred to the structure analysis as the boundary condition and the structure side is calculated until the convergence is reached as shown in Figure 2 (a).

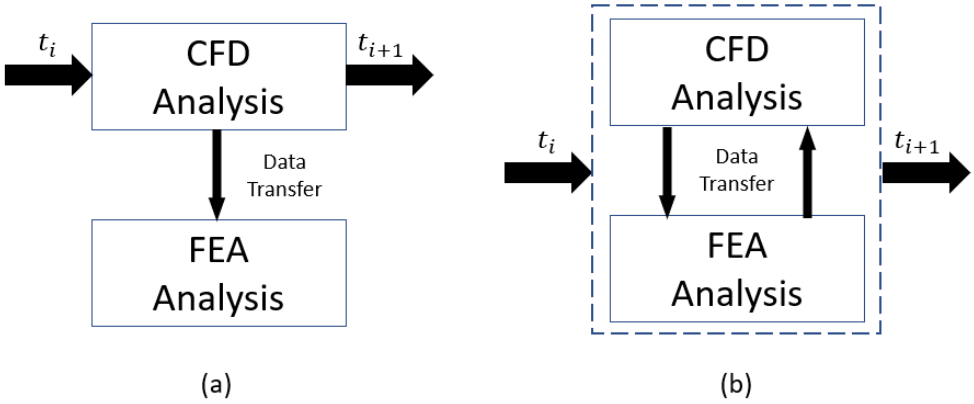


Figure 2 FSI coupling methods (a) one-way (b) two-way

In contrast, for the two-way coupling method, the fluid field is solved using CFD until the convergence criteria are reached. The aerodynamic pressures on the wing obtained from CFD solution are then mapped to the FEA model as load boundary conditions. After that, the FEA analysis is performed to calculate the structural responses of the wing such as deformation and stress distributions subjected to aerodynamic loads, followed by it will be interpolated to the fluid mesh accordingly. This is regarded as one inner loop of the simulation and these steps are repeated until the changes in the flow forces and the structural displacements fall below a prescribed level of tolerance as shown in Figure 2 (b). In this study, the FSI problem of the inverted wing in ground effect is solved with a two-way coupling partitioned method provided by the ANSYS software as the workflow described in Figure 3, which presents a single iteration of the fluid-structure coupled process. The iterative procedure is repeated for several time step until the desired simulation time is reached.

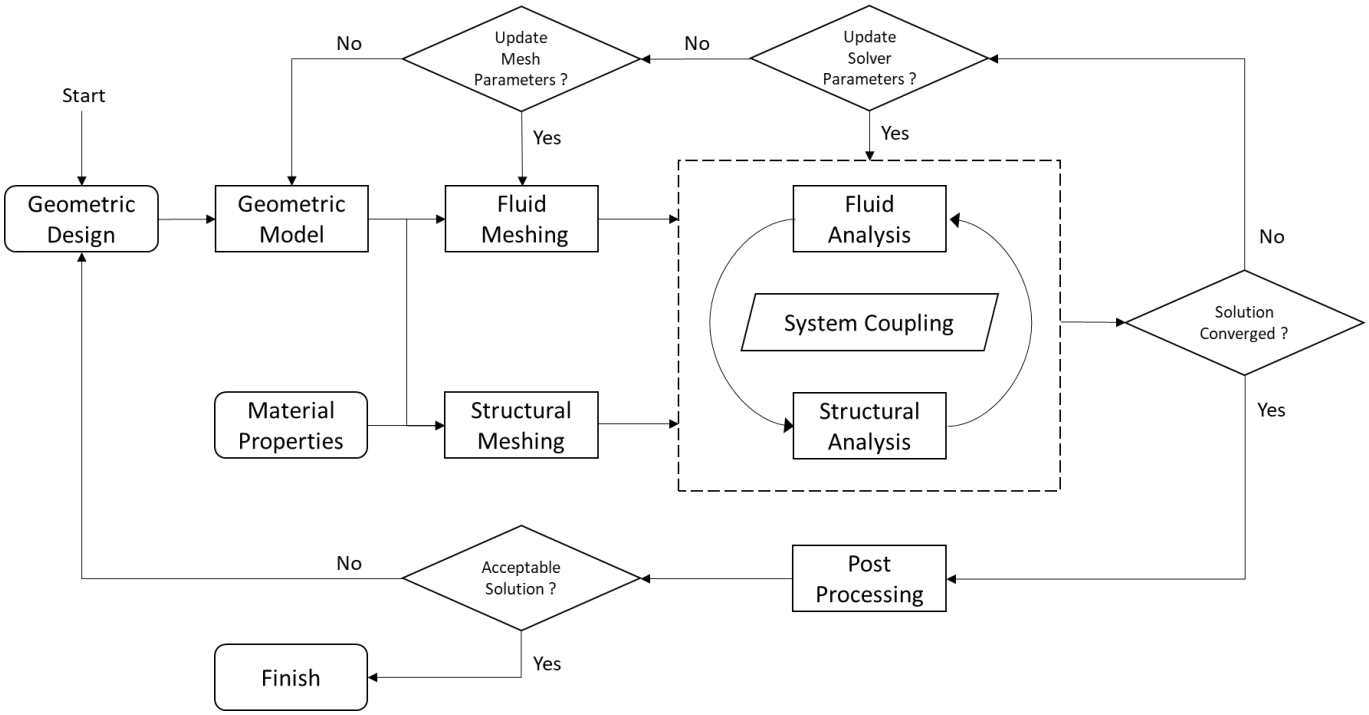


Figure 3 Workflow of Fluid Structure Interaction system

2.2 Geometry and mesh generation

The single element inverted wing used in this study is extracted from Zerihan's experiment [12]. A span and a chord are 1100mm and 223.4mm respectively. The cross section of the wing is a derivative of type LS (1)-0413 MOD shown in Figure 4 (a) and the details can be found in his study. The incidence of the wing is set at 3.45° and the height is defined by the vertical distance from the ground to the lowest point on the suction surface of the wing. To save computational resources, the half of the wing model is used for this study.

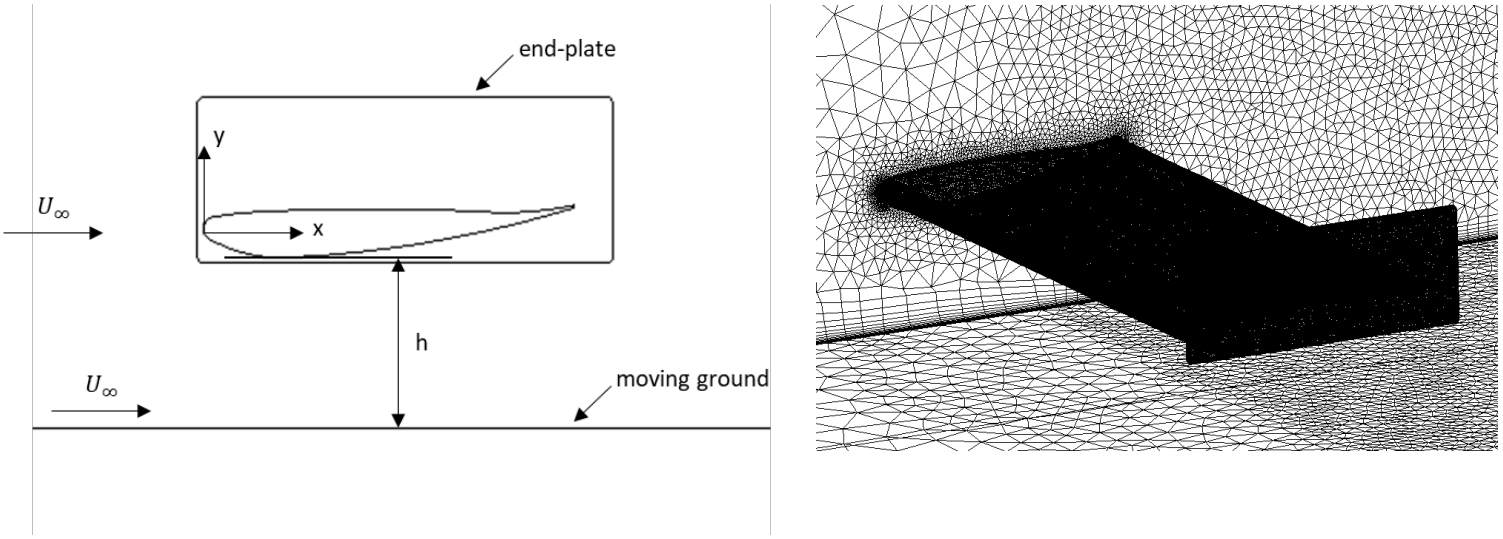
The computational grid is generated using ICEM CFD in ANSYS as presented in Figure 4 (b). A multiblock hybrid mesh is implemented containing both structured and unstructured grids and the relative grid topology and structure is maintained at various

ride heights. Prism layers are applied to capture the boundary layer of the wing and the ground accurately and the remainder of the domain is generated with unstructured tetrahedral mesh. Refinement is applied on areas of interest. For accurate investigation of the wake profile, additional structured fine density box is positioned directly behind the trailing edge of the wing. The first height cell within the boundary layer blocks of the wing and the ground is calculated using the equation (2) and set as y+ ≈ 1.

$$y^+ = \frac{yu_T}{\nu} \tag{2}$$

Where y is the distance to the wall, u_T is friction velocity, and ν is the kinematic viscosity

The total number of cells is varied according to the ride height and generally each case included approximately 9 million cells with majority of those placed towards the trailing edge of the wing and the wake box. For the structural analysis, the wing model is meshed using surface elements in ANSYS Mechanical.



(a) (b)

Figure 4 A single element wing in ground effect (a) schematic (b) computational grid

2.3 Computational setup

2.3.1 Fluid model

Numerical analysis for the fluid dynamics is performed using a RANS and is calculated via a centralized Linux-based cluster. All simulations are set up at ANSYS Fluent with steady-state 3D segregated configuration obtained by solving the Reynolds-averaged Naiver-Stokes equations. Upwind discretisation scheme is used for all cases, which are satisfied with second-order accuracy. The coupled pressure-velocity coupling algorithm is applied, which is considered compatible with coupling application including the structural analysis. Six turbulence models investigated with appropriate wall treatments and corresponding variants. The six turbulence models were used; the one equation Spalart-Allmaras model [16], the standard k-ε model [42], the standard k-ω model [43],

the k-ω SST model [17], the k-ε RNG model [44], and the Realizable k-ε model [45]. Enhanced Wall Treatments are applied on all k-ε model variants.

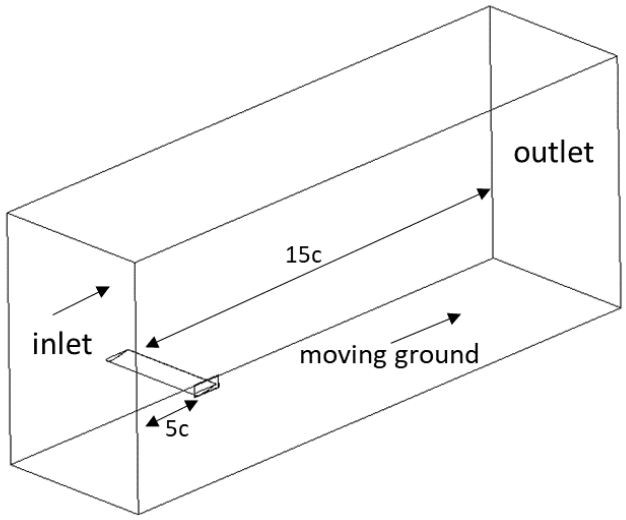


Figure 5 A schematic of computational domain

As shown in Figure 5, the boundary conditions are established to replicate the experiment configuration. The upstream boundary located upstream 5c from the leading edge is modelled using a velocity inlet boundary condition with 30 m/s uniformly distributed freestream in positive streamwise direction. The downstream boundary placed 15c downstream from the trailing edge is modelled using a pressure outlet boundary condition with gauge pressure of 0 Pa. The wing and the ground are modelled using a solid wall with no-slip condition. In addition, a tangential velocity equal to the freestream is imposed on the ground in order to represent a moving ground. The remainder of boundary conditions are modelled as a symmetry condition to impose zero crossflow condition and to remove the requirement of additional boundary layer resolution.

2.3.2 Structural model

In order to investigate the deflection of the inverted wing under aerodynamic loading, the wing is modelled with layered composite structure in ANSYS Composite PrepPost (ACP). The material used is Epoxy Carbon UD (230GPa) Prepreg provided by ANSYS Engineering Data Library, characterised by the mechanical properties shown in Table 1. ANSYS Mechanical is used to carry out the structural analysis using the finite element technique.

Table 1 Mechanical properties

Mechanical property	Value
Young's Modulus (E)	1.21E+05 MPa
Shear Modulus (G)	4700 MPa
Poisson's ratio (v)	0.27
Density (ρ)	1490 kg/m^3

3. RESULTS AND ANALYSIS

3.1 Grid sensitivity analysis

First of all, the grid convergence study is conducted in order to make sure that the numerical uncertainty generated by computation solution is within asymptotic range of convergence. The Grid Convergence Index (GCI) suggested by Roache [46–48] is used to provide consistent and reliable results of the grid convergence. The Table 2 indicates the grid information with three different mesh grids and the resulting drag coefficients computed from the solutions. Each solution is properly converged with respect to iterations. Using 16 cores of the high computing system power, the computational time for each mesh is as follows: 1.44 hours for the coarse mesh, 3.68 hours for the medium mesh and 8.56 hours for the fine mesh.

Effective grid refinement ratio is calculated using total number of grid points (N) and dimension of the fluid domain. The order of grid convergence, *P*, is 1.64. The GCI values for the drag coefficient are 0.27% and 0.85% for the coarse-medium and medium-fine grid respectively. The GCI ratio is 1.005 which means that the solutions are in the asymptotic range of convergence. Therefore, based on the GCI study, it can be shown that discretisation error is improved with the grid refinement.

Table 2 Summary of GCI study

Variable	Coarse	Medium	Fine
N	1.7M	3.2M	6.1M
Cd	0.0560	0.0558	0.0545
$r_{effective,12}$		0.81	
$r_{effective,23}$		0.82	
P		1.64	
GCI_{12}[%]		0.27	
GCI_{23}[%]		0.85	
GCI ratio		1.005	

In addition to the GCI study, the effect of grid sensitivity on the surface pressure distribution and wake survey at x/c = 1.2 is shown in Figure 6. There is little difference in the surface pressure distribution, but the coarse grid does not capture enough velocity deficit in the wake survey. In this study, as efficiency of computational resources is taken into consideration, the medium grid is eventually selected for all cases.

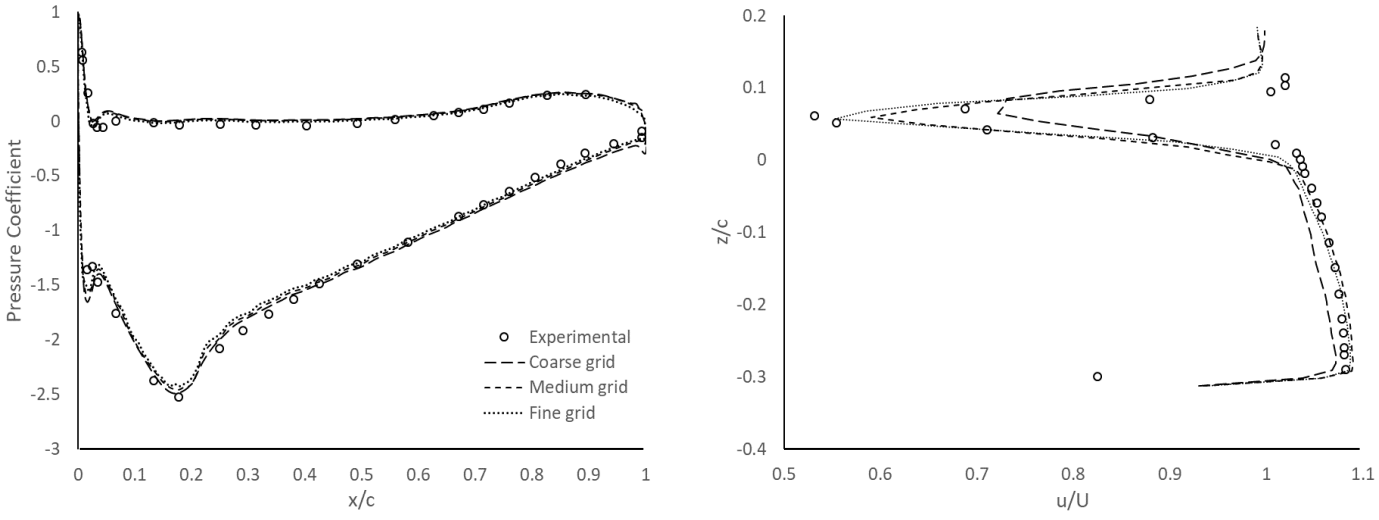


Figure 6 Effect of grid sensitivity (a) surface pressure distributions and (b) wake profiles at x/c = 1.2

Moreover, as the grid convergence of the fluid domain is investigated, mesh sensitivity study for structural analysis is also carried out. However, it is realised that the number of cells composed of surface mesh is too small to have an influence on performance of the wing compared to that of fluid domain in case of interaction between fluid and structure dynamics. Therefore, coarse mesh is selected for the structure modelling.

3.2 FSI analysis

3.2.1 Turbulence model study

Abovementioned, six different turbulence models are studied and for clarification, two cases are selected (h/c = 0.224 and 0.09). h/c = 0.224 describes a typical flow condition where the ride height of the wing is in the force enhancement region [4] and h/c = 0.09 represents a large separation region on the suction surface near the trailing edge. It is discussed that each turbulence model is suitable for this study by using the surface flow features and wake characteristics.

Figure 7 (a) depicts all the turbulence models representing the common features of the surface pressures at h/c = 0.224 at the centre of the wing. The stagnation pressure near the leading edge is accurately predicted at 1.0 by all the turbulence models at x/c = 0.0022 on the pressure surface. Although little discrepancies are observed with regards to prediction of the suction peak and subsequent pressure recovery along the lower surface, overall trend and general features are captured appropriately by all turbulence models. The maximum suction appears at a point called *suction peak*. Table 3 presents

detailed information about the pressure coefficient at suction peak and its location gained by each turbulence model and compares FSI results with experimental data and 2D aerofoil numerical data. The suction peak and its location are better predicted by the CFD-FEA coupled model as large discrepancy is observed with the 2D CFD results due to lack of dimensionality.

Figure 7 (b) shows wake profile results at x/c = 1.2 comparing the FSI numerical data with the experimentation, which was measured by Zhang and Zerihan [14] using Laser Doppler Anemometry (LDA) technique in a wind tunnel. The most accurate prediction of the wake profile is obtained with the Realizable k-ε model, which correctly predicted the velocity deficit within the ground boundary layer and the wake as well as the wake thickness. The comprehensive analysis of the wake characteristics captured by individual turbulence model is listed in Table 4. The k-ω SST model and the Realizable k-ε model are selected for further study as the most acceptable prediction is achieved.

Figure 7 (c) shows the surface pressure distribution at h/c = 0.09, observing a larger constant plateau is observed near the trailing edge compared to the greater height, which indicates early separated flow on the suction surface. It is found that the best prediction of the surface pressure is provided with the k-ω SST model between a variety of other turbulence models. Finally, the numerical results of wake measurement are presented in Figure 7 (d), however there is no experimental wake data at this height. It is speculated that the trend between the turbulence models is analogous to those at higher ride height.

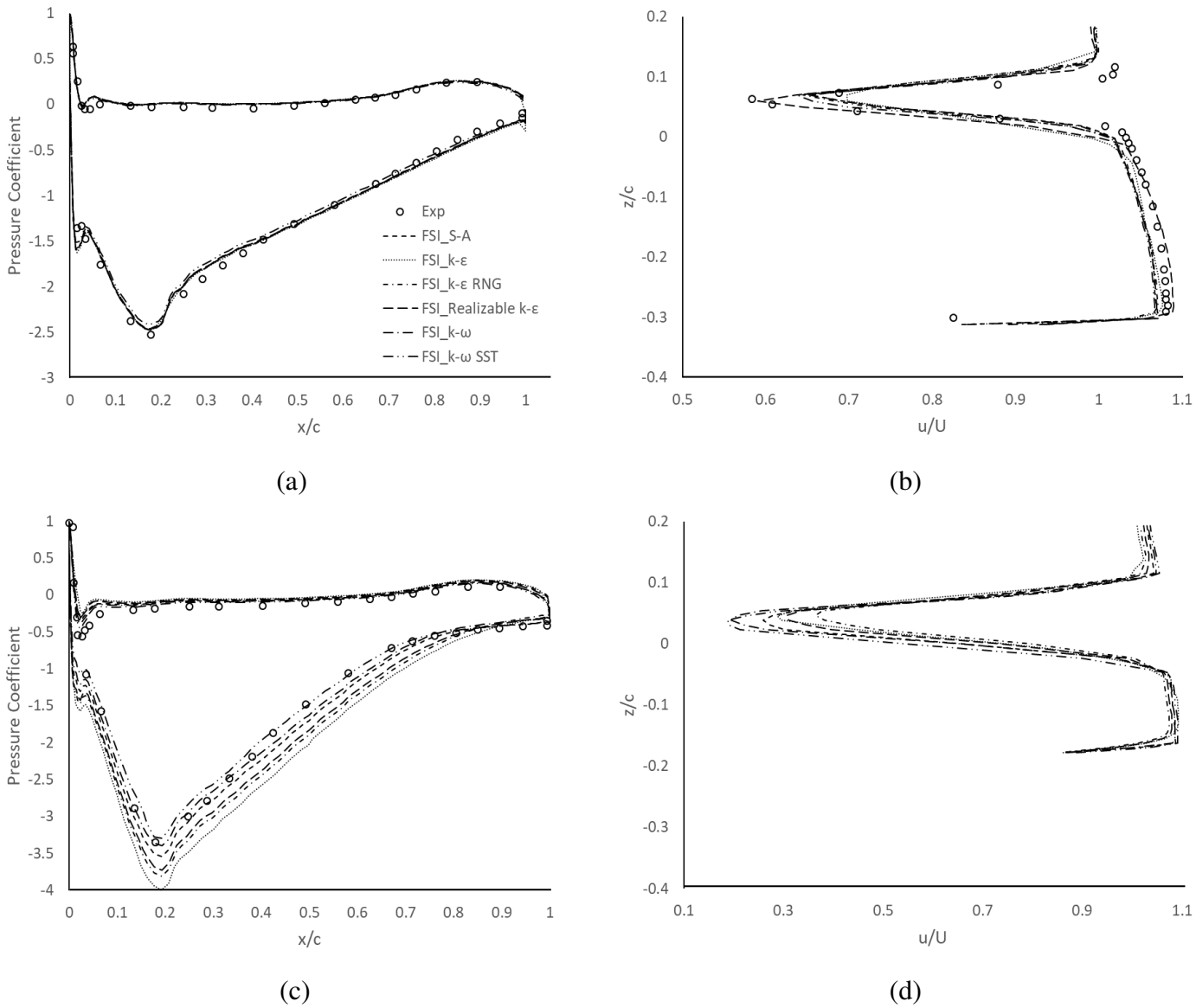


Figure 7 Effect of turbulence model variation (a) surface pressure distribution at h/c = 0.224, (b) wake profile at x/c = 1.2 for h/c = 0.224, (c) surface pressure distribution h/c = 0.09, (d) wake profile at x/c = 1.2 for h/c = 0.09

Table 3 Surface pressure information for various turbulence models, h/c = 0.224

	2D [7]		3D [11]	
	$C_{P_{suc}}$	x/c at $C_{P_{suc}}$	$C_{P_{suc}}$	x/c at $C_{P_{suc}}$
Experimental	-2.53	0.18	-2.52	0.18
Turbulence model	2D CFD [19]		3D FSI	
	$C_{P_{suc}}$	x/c at $C_{P_{suc}}$	$C_{P_{suc}}$	x/c at $C_{P_{suc}}$
Spalart - Allmaras	-2.92	0.19	-2.47	0.18
Standard k - ε	-2.92	0.19	-2.47	0.17
k - ε RNG	-2.81	0.19	-2.47	0.18
Realizable k - ε	-2.94	0.19	-2.46	0.18
Standard k - ω	-2.97	0.19	-2.46	0.18
k - ω SST	-2.92	0.19	-2.46	0.18

Table 4 Wake information for various turbulence models at x/c = 1.2 for h/c = 0.224

Turbulence model	u_{min}/U_{∞}	y/c at u_{min}	y/c at δ_{top}	y/c at δ_{bottom}	δ_{99}/c
Experimental	0.53	0.06	0.09	0.02	0.07
Spalart - Allmaras	0.65	0.07	0.10	0.02	0.08
Standard k - ε	0.69	0.07	0.10	0.02	0.08
k - ε RNG	0.65	0.07	0.10	0.02	0.08
Realizable k - ε	0.59	0.06	0.10	0.02	0.08
Standard k - ω	0.65	0.07	0.12	0.02	0.10
k - ω SST	0.64	0.07	0.12	0.02	0.10

3.2.2 Chordwise Surface pressures

The effect of various ride heights concerning the surface pressure distribution is investigated in comparison with the experimental pressures [12]. The chordwise surface pressures at the centre of the wing are presented in Figure 8 for only two ride heights h/c = 0.313 and 0.134 for fair comparison, provided by the k-ω SST and the Realizable k-ε models respectively. In general, the computational surface pressures show good agreement with the experimental pressures with both turbulence models for all heights. The leading-edge stagnation point is accurately captured at x/c = 0.0022. The suction spike is observed at x/c = 0.019 for both turbulence models and the magnitude is slightly increased with ride height reduced. However, the experimentation doesn't present this leading-edge suction spike due to discontinuous pressure data points measured. The suction peak is constantly observed at x/c = 0.192 and the magnitude is increased with lowered ride height. Downstream of the suction peak, the pressure on the lower surface started to recover up to the trailing edge. When the ground is approached, the suction is increased owing to the flow acceleration, which shows that the substantial pressure gains on the suction side is achieved as shown from the suction peak to x/c = 0.4, where the wing is at the lowest position with the most accelerated airflow. The overall rate of the pressure recovery along the suction surface is captured in an accurate manner with the k-ω SST model. On the other hand, overprediction of the pressure recovery rate is observed with the Realizable k-ε model at h/c = 0.09, causing inaccurate pressure difference at the trailing edge. Therefore, the k-ω SST model offers better prediction with regard to surface pressure distribution, especially to the pressure recovery rate on

suction surface of the wing at lower ride height. The pressures on the pressure surface show little variation across the chord at all ride heights.

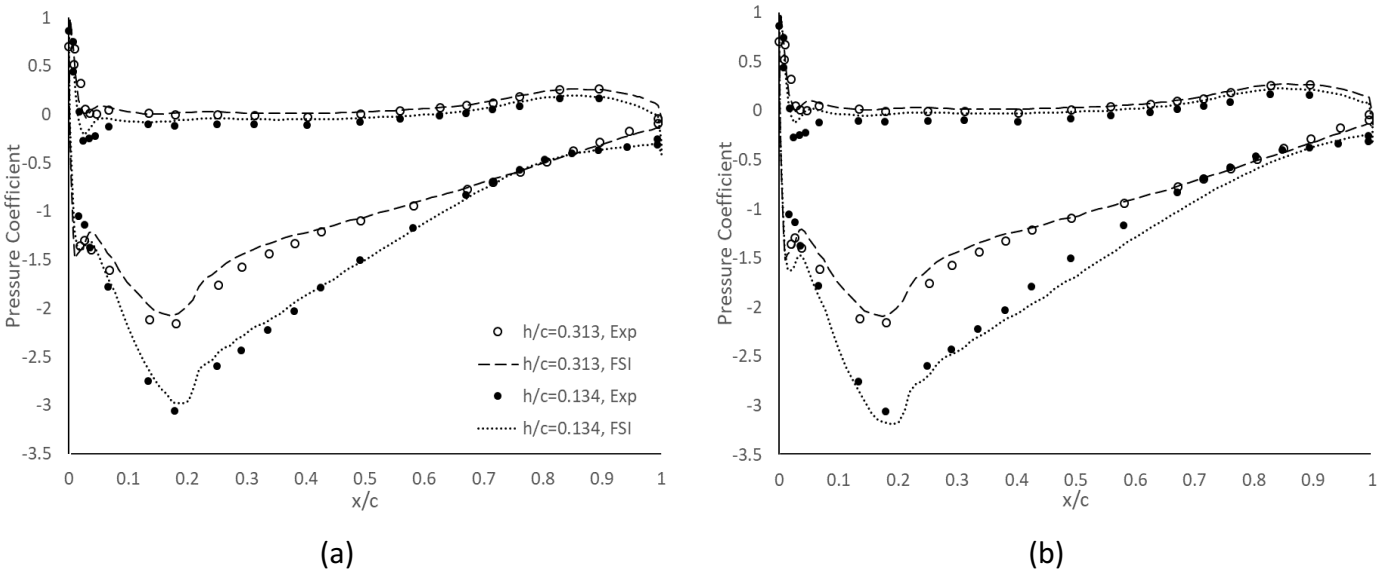
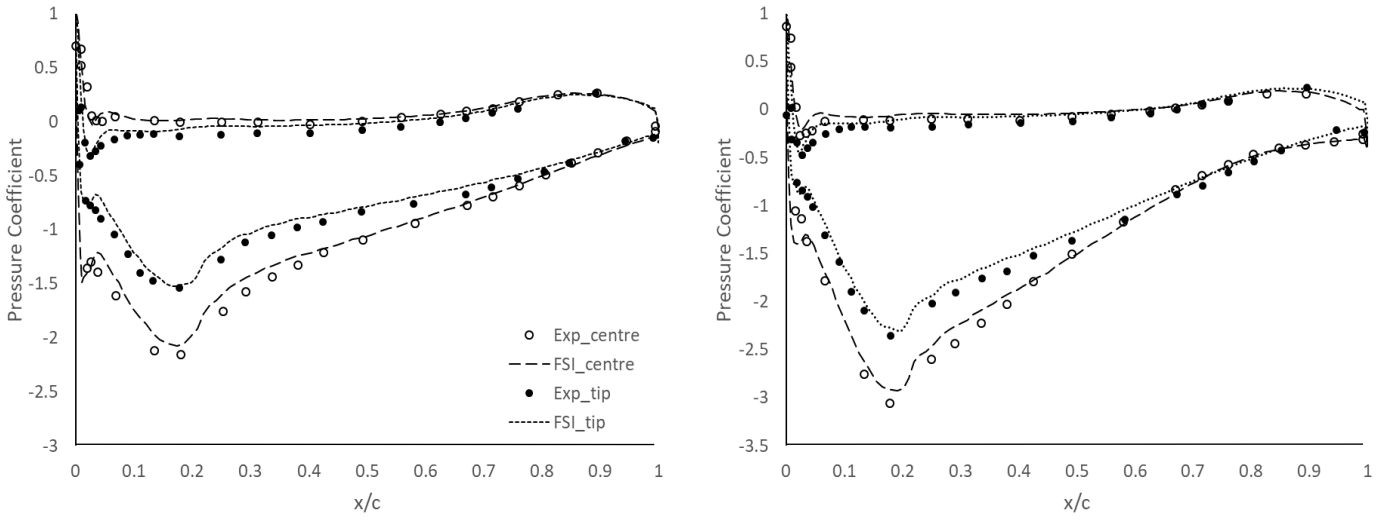


Figure 8 Chordwise surface pressure distribution at wing centre in ground effect at h/c =0.313 and 0.134 (a) k-ω SST model (b) Realizable k-ε model

Comparisons of the chordwise pressure at the centre of the wing and near to the tip for two ground heights of h/c = 0.313 and 0.134 generated by using k-ω SST model are presented in Figure 9. The agreement between computational and experimental results on the pressures is achieved. At a moderate height of h/c=0.313 shown in Figure 9 (a), the suction peak is slightly underpredicted at both locations and its magnitude is significantly decreased near to the wing tip. The suction peak is observed at x/c = 0.134 at the wing centre and at x/c = 0.179 at the wing tip. This could be indicative of the fact that the airflow around the wing tip can be at a lower effective incidence due to the wing tip vortex effect.

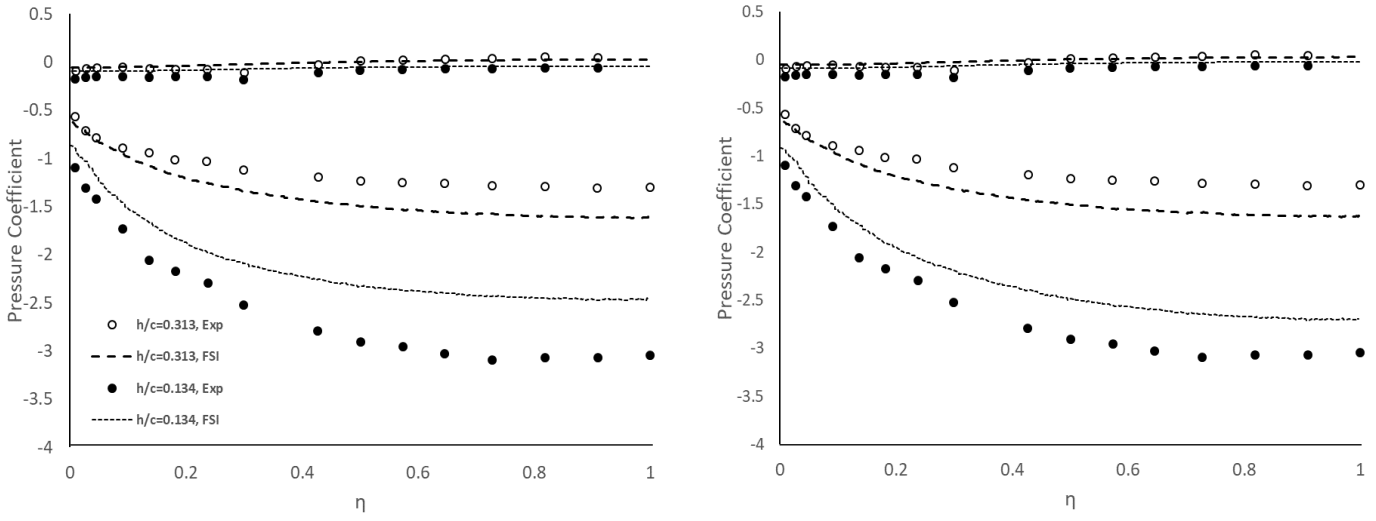
For the case at a lower ground height of h/c = 0.134 shown in Figure 9 (b), a similar trend is obtained. A considerable discrepancy of the suction loading in the suction surface between the wing centre and the wing tip is presented. Furthermore, the magnitude of the suction peak is relatively greater than the one at higher ride height, which indicates enhancement of the ground effect due to the lowered ground proximity. At this height, it is highlighted that the experimental pressures at the wing centre represent a region of flow separation near the trailing edge shown in terms of a shot scale of constant pressure, and it is accurately captured by the computational pressures. However, the surface pressure at the wing tip gained both experiments and FSI simulations do not exhibit this separation and one of significant factors is that the reduced circulation results in a smaller pressure recovery demand at the wing tip. The suction peak is observed at x/c = 0.18 for all locations.

It is expected that a greater suction peak would be gained by the FSI computational simulation compared to the experimental data. It is caused by the fact that this numerical approach is capable of describing dynamics of the wing characteristics in terms of deflection, enhancing the pressure difference due to greater flow acceleration caused by the ground effect when the wing is approached to the ground. However, at the same time, the wing is twisted when deformed, so that the increase in suction pressure loading could be cancelled out by decrease in the effective incidence due to the wing being backed off. Therefore, it is speculated that the FSI analysis show similar level of suction peak compared to the experiments.



(a) (b)

Figure 9 Chordwise surface pressures at wing centre and wing tip in ground effect generated by k-ω SST model (a) h/c=0.313 (b) h/c=0.134



(a) (b)

Figure 10 Spanwise surface pressures in ground effect for different ride heights (a) k-ω SST (b) Realizable k-ε

3.2.3 Spanwise surface pressures

Spanwise surface pressures at the quarter-chord location are investigated with regard to various ride heights using different turbulence models and compared between experimental and computational results shown in Figure 10, which highlights the three-dimensionality of the flow. Little variation of the pressure value on the pressure surface is observed as the ground height is reduced, whereas the suction loading on the suction surface increases as the ground is approached. It is found that greater amount of pressures is generated across the wingspan by the FSI simulation at h/c = 0.313 for all turbulence models, which means increase in downforce. It can be due to the stronger ground effect as the wing is temporarily deflected with increase in ground proximity. On the other hand, when the wing is lowered closer to the ground, h/c = 0.134, the computational pressures are underpredicted than the experimental pressures over the whole range of the wingspan for both turbulence models. In addition, the magnitude of this discrepancy is observed larger for the k-ω SST model. Flow separation phenomena appeared with constant pressure region near the trailing edge is not captured at the quarter-chord location as contrasted with the one shown in Figure 9 (b). It is caused by the fact that the separation point does not move this far forwards.

In this section, it can be discussed that lack of the surface pressures on the suction side across the wingspan at the lower ride height is observed with the FSI modelling. First, the effect of force reduction in ground effect becomes stronger. According to Zerihan and Zhang [12], as the ground height is decreased, the downforce is increased accordingly due to the ground effect. However, below a certain height, the slope of the

downforce starts to be levelled off and then falls off after reaching the maximum value, which is called force reduction region. Then, as the ground proximity between the wing and the ground is increased further, the loss of downforce becomes greater. With the wing deformed in accordance with elastic characteristic of composite structure, the influence of the force reduction region on wing performance becomes severe, resulting in more loss of loadings as we can see less surface pressure in Figure 10 (a). Secondly, it can be attributed to the reduction of effective incidence at the wing tip due to the wing tip vortex. The airflow around the wing tip is operated at a relatively lower effective incidence due to the upwash caused by the tip vortex effect. The wing is deflected and twisted on account of structural elasticity of the composite materials, which results in amplifying the effect.

3.2.4 Aerodynamic forces

Figure 11 shows the effect of non-dimensional ground heights on the downforce is quantified. The calculated downforce with different turbulence models is compared with the values measured experimentally [12]. In general, in accordance with the experimental results, as the wing is approached closer to the ground across large and moderate heights, the gradient of downforce is increased. As the ride height is further lowered within a range of small heights, the slope of the line starts to slow down and finally decline with the downforce reaching to a maximum level at around h/c = 0.111, corresponding to CL = 1.57. Comparing the results between provided by two turbulence models, the overall trend in downforce variation is observed more accurately with the k-

ω SST model as it is capable of capturing the reduction in downforce at small ride heights. On the other hands, consistent discrepancy between the experiment and the FSI results for all ride heights is observed with both turbulence models, which might be attributed to a lower effective angle of attack induced by the wing tip deflection and wing tip vortices. The Realizable k-ε model offers analogous tendency of the downforce as the experimentation within large ride heights. However, as the wing is approached further to the ground within a range of small ride heights, the downforce keeps increasing with the maximum value measured at the lowest height.

The calculated downforce with ride heights variation using the FSI modelling is quantified and compared with the experimental forces. Following the trend of the experimental results, the computational results increase gradually with decreasing ground heights across a range of large and medium heights and the gradient then starts to decrease by reaching a maximum of CL = 1.29 at h/c = 0.134 from the ground with the k-ω SST model, whereas CL = 1.52 at h/c = 0.09 with the Realizable k-ε model. The increase in downforce with decreasing the ground height can be explained by a summation of total pressures, which is the main contribution despite the three-dimensional effect. Aa the height is reduced, surface pressure on the lower surface of the wing increases as well as surface pressure on the upper surface does, which results in a maximum downforce when integration of total surface pressures is a maximum. Consistent difference of downforce between experimental and computational studies is noticed throughout variation of ground heights. Two reasons can be suggested for explaining the discrepancy of downforce as the wing ride height is reduced. It is likely

that a twist of the wing is the main factor. As a result of existence of the ground, the distance between the wing and the ground is not sufficient to enable the vortex to develop. For considering the wing deflection caused by the elastic characteristics of the composite structure, as the wing is deformed and approached closer to the ground than the rigid one, it can make the distance between the wing and the ground even shorter, hindering the vortex roll up. In addition, the wing is deflected under the aerodynamic loading and also tilted backwards, following by the airflow is approaching the wing at lower effective angle of attack than the rigid case, reducing the pressure difference between upper and lower surfaces and ultimately the downforce. Another possibility is that the wing deformation might affect adversely creation of the lower edge vortex. Structural deformation may contribute to deterioration of shear layer entrainment from outboard of the endplate to feed the vortex, which leads to weakening the strength of the vortex.

Similarly, the influence of various ride heights on the aerodynamic drag is shown in Figure 12. As the distance between the wing and ground is reduced, the downforce increases until the maximum value is achieved. This causes the induced drag of the wing and as a result the drag increases with decreasing the ride heights for moderate and large heights. However, at a range of ground heights, the drag continues to increase until it reaches a maximum whereas the downforce decreases after the peak point. It is speculated that the drag increase at small ride heights can be attributed to other reasons as the induced drag caused by the downforce is not enhanced within the force reduction region. The numerical analysis using the different turbulence models observes

a similar trend of the increase in drag force as the experimentation does. However, the discrepancy between experimental and computational results is also presented and the magnitude of the gap is decreased with increased ground proximity.

The drag gained from the numerical simulation increases for all ride heights in a similar manner to the experiments. However, the gap between experimental and computational results is observed and its magnitude is decreased as the ride height is lowered. At large and moderate ground heights, larger drag is generated by the computational solution due to greater amount of induced drag caused by enhancing the downforce due to the wing deflection. At the small heights, it is speculated that the increase in drag is not much affected by the wing deformation due to weakened vortex strength but caused by the separation at the trailing edge and vortex dilution in a similar manner to the experiment.

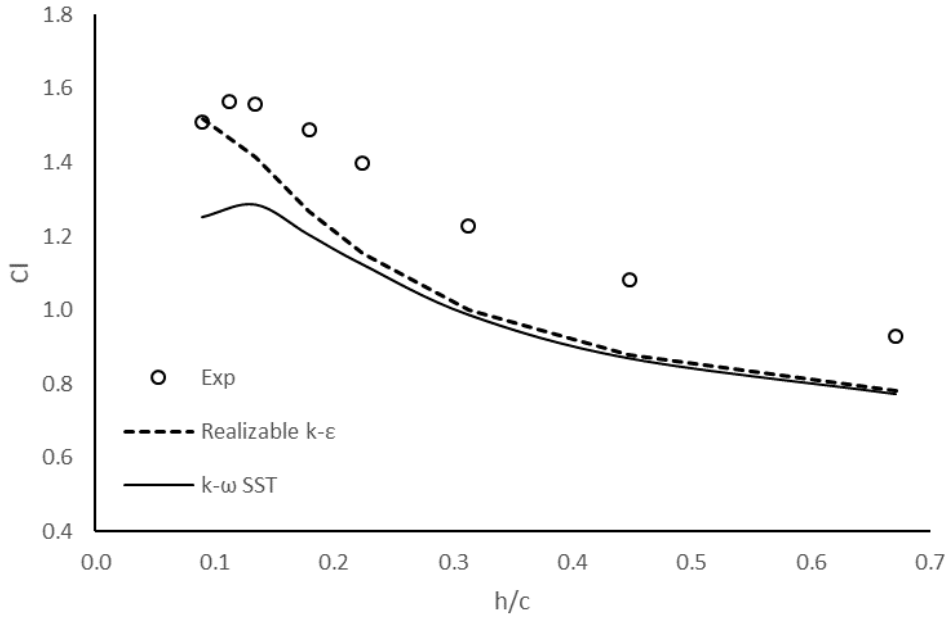


Figure 11 Downforce of single element wing in ground effect with various heights

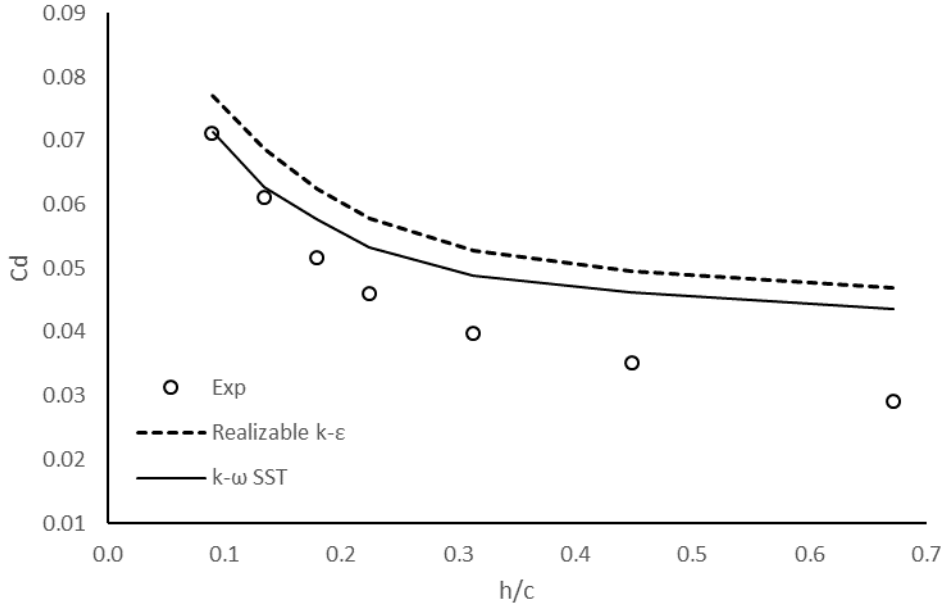


Figure 12 Drag of single element wing in ground effect with various heights

3.2.5 Wake flow field

In Figure 13, u/U velocity contours obtained from computational analysis are presented for heights of the h/c = 0.448, 0.224, 0.134, and 0.09 in order to study the wake characteristics of the wing and near-field flow, which is in the region of x/c = 1.0 – 1.5. The black lines represent the rear portion of the wing and the endplate. Compared to the experimental result performed by the Laser Doppler Anemometry (LDA) technique [49], numerical results show analogous tendency as presented. In general, the flow field of the wake is shown to change as the ride heights are varied. It can be also seen that the flow is accelerated (in red) between the trailing edge and the ground and is decelerated downstream of the trailing edge due to the adverse pressure gradient. At the h/c = 0.224 and 0.134, a small region at the rear of the trailing edge

shows a negative velocity (in blue), indication of reversed flow, and this region becomes more obvious with increasing the ground proximity. For the h/c = 0.09, it is observed that the negative velocity region becomes considerably larger and its size is increased as the ground height is lowered. In addition, the path of the wake is assessed with decreasing ride heights. For the h/c = 0.448 and 0.224 cases, the wake behind the trailing edge follows an upward line of the angle of attack of the wing as it goes downstream. For the h/c = 0.134 case, where flow is separated, the path of the wake is likely to start levelling off. At the lowest height h/c = 0.09, flow separation occurs to a great extent and the path is leaned more towards a horizontal line. The size of the wake is also changed with the ground height variation. As the distance between the wing and the ground is reduced, the downforce is increased due to the flow acceleration. Accordingly, the adverse pressure gradient is increased, which results in increasing the boundary layer thickness. When observing the wake profile at the h/c = 0.448 and at h/c = 0.09, the size of the velocity deficit is considerably increased as the ground height is lowered. In comparison with the experimental result, computational analysis presents velocity profile with slightly higher speed between the wing and the ground, which can be attributed to increasing flow acceleration caused by the wing deflection. The larger size of the velocity deficit region is observed with the FSI simulation It is believed that it may be wing deformation to deteriorate the vortex-induced effect and to develop the effect of adverse pressure gradient, which could cause larger separation.

Figure 14 presents the profiles of the relative velocity at a streamwise location of x/c = 1.2, provided by the experimental and computational method. Only three ride heights

are included in this Figure which have available experimental data. The detailed information about the wake profiles is given in Table 5. In general, both turbulence models show good agreement on prediction of the wake profile with the experimental data. The two models accurately predict the velocity deficit near the ground boundary layer and the wake thickness with decreasing the ride heights. As representing the marginal overprediction of velocity deficit within the wake and top wake boundary and slight underprediction of the lower wake boundary thickness simulated by both turbulence models, it is believed that the computational results provide larger size of the wake profile, which can be caused by increasing the adverse pressure gradient due to the wing deflection. The k-ω SST model slightly overpredicts the gradient of velocity recovery toward the upper wake, resulting in an overprediction in the wake thickness. The Realizable k-ε model shows similar tendency of wake profile prediction with a certain extent of underestimation in the upper boundary and in the ground boundary layer. Accordingly, the k-ω SST model produces better prediction of the wake profile with more accuracy.

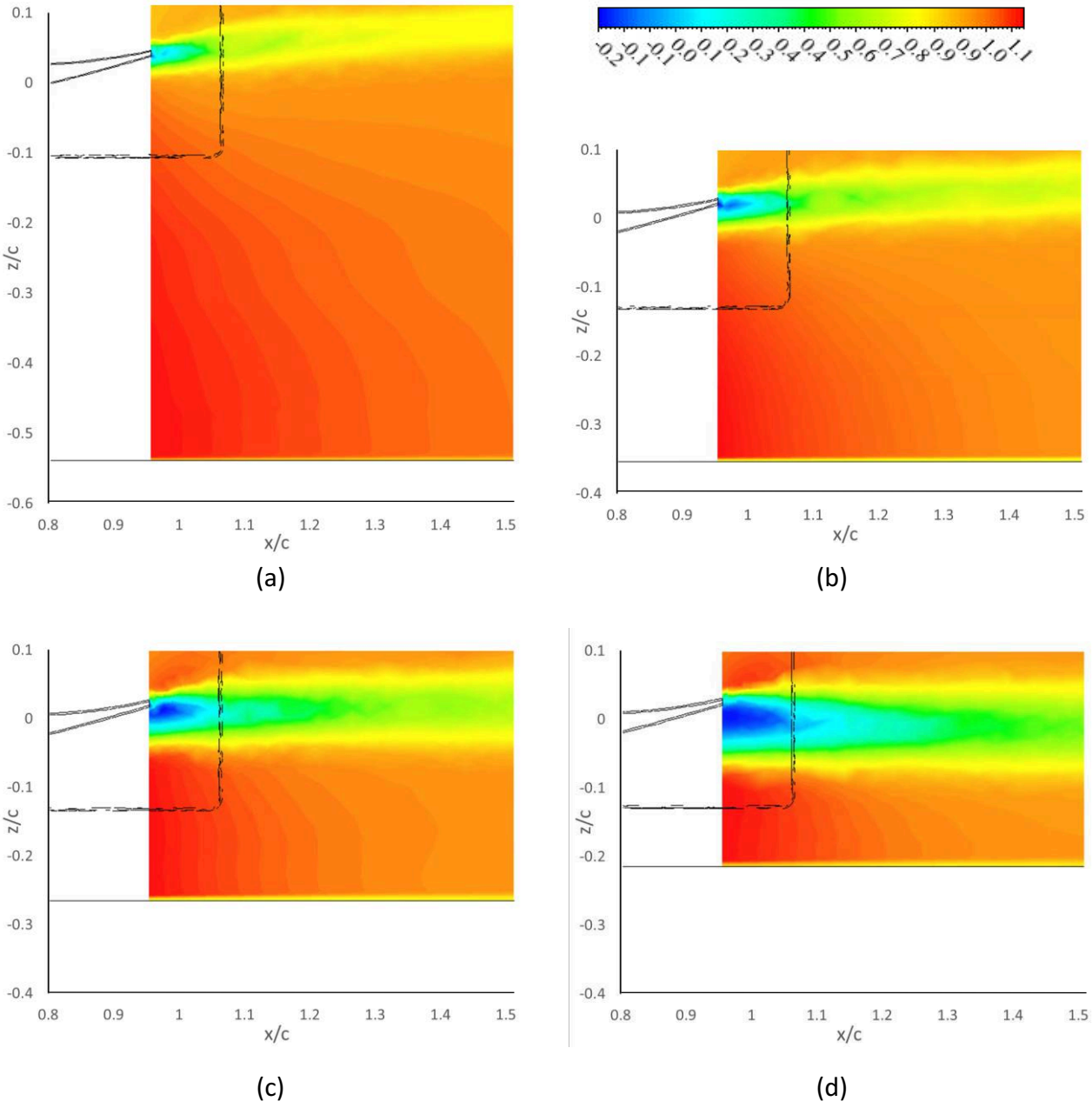
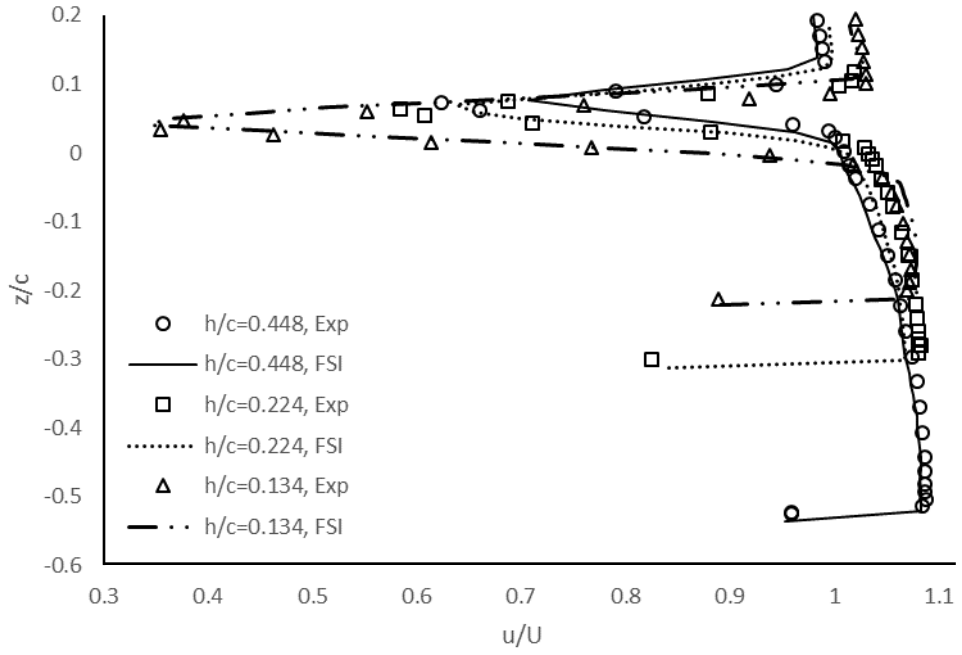
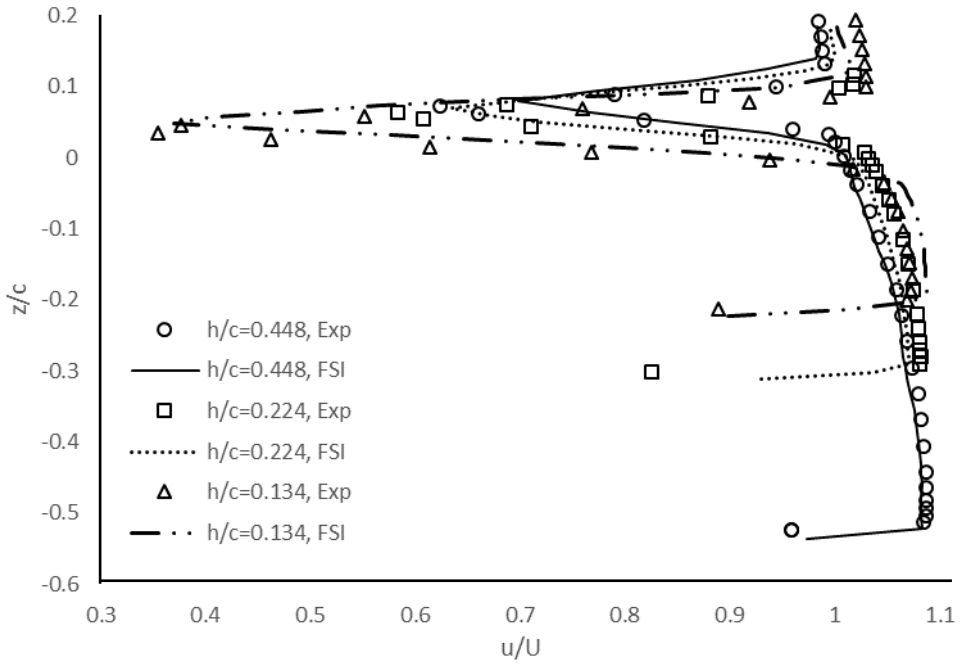


Figure 13 u/U velocity contours at various heights (a) h/c = 0.448, (b) h/c = 0.224, (c) h/c = 0.134, h/c = 0.09



(a)



(b)

Figure 14 Wake profile at x/c = 1.2 (a) k – ω SST and (b) Realizable k – ε

Table 5 Wake information for various ride heights at x/c = 1.2

h/c	Exp/FSI	u_{min}/U_{∞}	y/c at u_{min}	y/c at δ_{top}	y/c at δ_{bottom}	δ_{99}/c
0.448	Exp	0.62	0.07	0.10	0.03	0.07
	k – ω SST	0.70	0.08	0.12	0.02	0.11
	Realizable k – ε	0.70	0.08	0.12	0.02	0.11
0.224	Exp	0.58	0.06	0.09	0.02	0.07
	k – ω SST	0.64	0.07	0.12	0.02	0.10
	Realizable k – ε	0.63	0.07	0.11	0.02	0.09
0.134	Exp	0.35	0.03	0.09	-0.02	0.11
	k – ω SST	0.34	0.04	0.10	-0.01	0.11
	Realizable k – ε	0.37	0.04	0.11	-0.01	0.12

3.3 Structural analysis

Structural analysis of the single element composite wing is performed with variation of composite structure. In this study, in order to investigate the aeroelastic effect under the condition of realistic application, the span of the wing is extended up to 900mm, compared to the previous models, being based on F1 2018 technical regulation [50] and the airflow coming from the inlet boundary for CFD analysis speeds up to 80 m/s which is regarded as high speed range in F1. The k-ω SST turbulence model is used under the free stream condition (no ground effect), which is intended to investigate the influence on aerodynamic performance only made by the structural characteristics. The most common material used in the motorsport industry is Carbon Fibre Reinforced Polymer

(CFRP) and the main material for this study is chosen to be a carbon/epoxy prepreg. The mechanical properties of uni-directional (UD) and woven prepreg are taken from the Ansys Composite Library [51] and the structure of the composite wing is created by the ANSYS Composite Prepreg. Table 6 presents a variety of composite structures in terms of different manufacturing structure (uni-directional and woven), ply orientation, and different core materials. The effects of the composite structure characteristics on the wing deflection and maximum stress are presented in the Figure 15 and additionally aerodynamic performance and weight results are shown in Table 6. The conclusion can be drawn as follows.

Comparing the UD cases with woven fabric cases, for example case 1 and 2, the wing constructed with UD structure shows more deflection of 19.2 mm and twice larger max stress shown in Figure 15, which means that the woven laminate structure has higher stiffness leading to less aeroelastic effect. Table 7 presents that the woven structured wing generates higher downforce and drag compared with the UD composite; however, difference of aerodynamic efficiency between two structures is marginal. It is concluded that, despite weight penalty, the woven structure can achieve better aerodynamic performance to avoid greater disturbance of flow field around the wing caused by larger deformation, maintaining good structural stability.

The composites structures are composed of changing ply orientations to evaluate its influence on the aerodynamic and structural performance, for example case 2 and 3 shown in Table 5. The results show that little increase in max deflection and max stress is achieved using the set [0/45] for the pile orientation shown in Figure 15 and it is

speculated that the cross-ply orientation has little influence on the structural performance when most of the aerodynamic force applied on the wing is perpendicularly exerted. Along the same line, Table 6 presents that no significant changes are observed for the aerodynamic forces and efficiency by changing a sequential cross-ply orientation.

For designing the composite wing, core material can be often utilised in order to take structural advantages such as total weight reduction and strengthened mechanical characteristics. In this study, two core materials widely used in motorsport industry are evaluated, which are nomex honeycomb and aluminum honeycomb. First, by comparing cases between nomex and aluminum, decrease in max deflection and max stress is observed using the wing with aluminum honeycomb (case 7,8 and 9). However, the results describe that there is slight increase in total wing weight for the aluminum cases, followed by analogous level of aerodynamic performance. In comparison with the no core wing situation (cases 1, 2 and 3), significant weight reduction by 15% for UD and 22 % for woven fabric is achieved for utilising the aluminum structure replacing a couple of layer of CFRP, despite no substantial changes in aerodynamic performance and max stress. Likewise, it is shown that the nomex core results in similar consequences as the aluminum cases, obtaining substantial reductions in weight by 20% for UD and 24% for woven fabric. In summary, it is concluded that the core material could provide structural advantages of mechanical characteristics under the same amount of fluid loading as the no core structure, keeping the equivalent level of aerodynamic performance and weight benefit.

Table 6 Variation of composite structure for single element wing

Case	1	2	3	4	5	6	7	8	9
Material	UD	Woven 0/90	Woven 0/45	UD	Woven 0/90	Woven 0/45	UD	Woven 0/90	Woven 0/45
ply1	0	0/90	0/45	0	0/90	0/45	0	0/90	0/45
ply2	90	0/90	0/45	90	0/90	0/45	90	0/90	0/45
ply3	0	0/90	0/45	0	0/90	0/45	0	0/90	0/45
ply4	90	0/90	0/45	90	0/90	0/45	90	0/90	0/45
ply5	0	0/90	0/45						
ply6	90	0/90	0/45						
ply7	90	0/90	0/45	Nomex honeycomb			Aluminum honeycomb		
ply8	0	0/90	0/45						
ply9	90	0/90	0/45	90	0/90	0/45	90	0/90	0/45
ply10	0	0/90	0/45	0	0/90	0/45	0	0/90	0/45
ply11	90	0/90	0/45	90	0/90	0/45	90	0/90	0/45
ply12	0	0/90	0/45	0	0/90	0/45	0	0/90	0/45

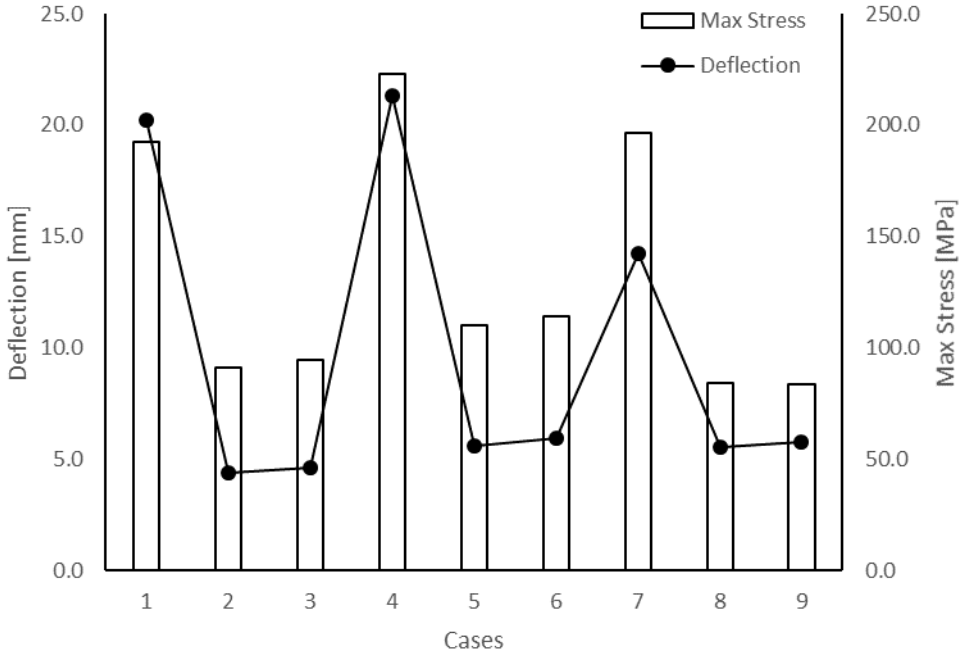


Figure 15 Result of deflection and mass stress of single element composite wing with various composite structure

Table 7 Results of aerodynamic performance and weights with various composite structure

Case	1	2	3	4	5	6	7	8	9
Material	UD	Woven 0/90	Woven 0/45	UD	Woven 0/90	Woven 0/45	UD	Woven 0/90	Woven 0/45
	No core			Nomex honeycomb			Aluminum honeycomb		
CL	0.774	0.811	0.815	0.761	0.782	0.784	0.778	0.785	0.785
Cd	0.034	0.036	0.036	0.033	0.035	0.035	0.034	0.035	0.035
L/D	22.95	22.65	22.48	22.87	22.66	22.66	22.78	22.62	22.62
Weight [kg]	1.13	1.97	1.97	0.90	1.49	1.49	0.96	1.54	1.54

4. CONCLUSION

In this study, a methodology was explored to perform a Fluid-Structure Interaction analysis for the aeroelastic behaviour of a single element inverted composite wing including the ground effect. The analysis was carried out by a two-way steady-state iteratively implicit coupling approach using the commercial software package ANSYS in conjunction with the high-performance cluster. The FSI model demonstrated the effect of structural elastic deformation of the wing on the aerodynamic performance at various ride heights compared with the experimental results.

According to in-depth investigation shown in the surface pressure distribution, sectional forces and wake profile, computational results achieved good overall agreement in comparison with the experimental data. It also showed the validity of numerical approach with a FSI model. Fluid domain size was determined as a result of the grid sensitivity study and various turbulence models were evaluated and compared in consideration of flow field characteristics. As a consequence, the most accurate prediction of the surface pressure and sectional forces were obtained with the k-ω SST turbulence model. Furthermore, this model presented more accurate results concerning the wake flow field, in particularly the lower wake boundary and offered better understanding of the wall jet prediction.

The effect of various ride heights concerning the surface pressure distribution and aerodynamic forces were investigated in a numerical approach using the FSI model and compared with the experimental results. Good overall agreement between computational and experimental chordwise surface pressures was achieved at

moderate and lower ride height level. For spanwise surface pressure, there was little variation of the pressure value on the pressure surface regardless of ride height change. FSI numerical solution generated greater amount of suction pressure on the suction surface at the moderate height due to enhanced ground effect compared to the experiment. Conversely, the computational pressures were underpredicted at the lower height. It was speculated due to significant effect of force reduction region caused by the wing deflection and reduction of effective incidence at the wing tip.

Aerodynamic forces with a range of various ground heights were studied using FSI model. It was observed that the numerical method generated less downforce compared to the experiment, which may be caused by reduced effective angle of attack due to the wing deflection and deterioration of vortex-induced effect. In addition, greater increase in drag was obtained by the FSI simulation, which might result from increment of induced drag caused by the wing deformation and separation at the trailing edge. The influence of varied composite structures on the aero and structural performance of the wing was extensively assessed. It can be seen that despite weight penalty, the woven structure demonstrated achievement of better aerodynamic performance caused by larger deformation, maintaining good structural stability. Implementation of core material provided significant structural advantages of mechanical characteristics, keeping the equivalent level of aerodynamic performance and weight benefit.

NOMENCLATURE

c	Chord
CL	Sectional lift coefficient
Cp	Coefficient of pressure
Cpstag	Coefficient of pressure at the leading-edge stagnation point
Cpsuc	Coefficient of pressure at maximum suction
h	Ride height
L	Lift, positive indicates downforce i.e. force in a negative z direction
p	Static pressure
q∞	Dynamic head
t	Time
umin	Minimum u velocity component in wake
U	Freestream velocity
x, y	Cartesian coordinates, x positive downstream, y positive upward
xsep	Suction surface separation point
y+	Nondimensional length
α	Incidence of aerofoil, positive for a nose down rotation
δbottom	Bottom of wake thickness
δtop	Top of wake thickness

$\delta 99$	Wake thickness as measured by 99% displacement thickness
μ	Viscosity
ρ	Density
∞	Freestream

REFERENCES

[1] Agathangelou, B. and G., 1998, “Aerodynamic Considerations of a Formula 1 Racing Car,” SAE Publ., p. 980399.

[2] Castro, X., and Rana, Z. A., 2020, “Aerodynamic and Structural Design of a 2022 Formula One Front Wing Assembly,” Fluids.

[3] Somerfield, M., 2016, “‘Analysis: Is F1 Set for Another Flexi-Wing War?,’” Motorsport.com.

[4] Katz, J., 1985, “Calculation of the Aerodynamic Forces on Automotive Lifting Surfaces,” ASME J. Fluids Eng., **107**, pp. 438–443.

[5] Katz, J., 1994, “Considerations Pertinent to Race-Car Wing Design,” *Loughborough University Conference on Vehicle Aerodynamics*, pp. 23.1-23.7.

[6] Katz, J., 1995, “High-Lift Wing Design for Race-Car Applications,” SAE Publ., p. 951976.

[7] Knowles, K., Donahue, D., and Finnis, M., 1994, “A Study of Wings in Ground Effect,” *Loughborough University Conference on Vehicle Aerodynamics*, pp. 22.1-22.13.

[8] Ranzenbach, R., and Barlow, J. B., 1994, “Two-Dimensional Airfoil in Ground Effect, an Experimental and Computational Study,” SAE Tech. Pap., (94–2509).

[9] Ranzenbach, R., and Barlow, J. B., 1995, “Cambered Airfoil in Ground Effect- Wind Tunnel and Road Conditions,” 13th Appl. Aerodyn. Conf., pp. 1208–1215.

[10] Ranzenbach, R., and Barlow, J., 1996, “Cambered Airfoil in Ground Effect-an Experimental and Computational Study,” SAE Tech. Pap., **960909**.

[11] Ranzenbach, R., Barlow, J. B., and Diaz, R. H., 1997, “Multi-Element Airfoil in Ground Effect- an Experimental and Computational Study,” AIAA Pap. no. 97-2238.

[12] Zhang, X., and Zerihan, J., 2000, “Aerodynamics of a Single Element Wing in Ground Effect,” AIAA J., **AIAA 2000**-.

[13] Zhang, X., and Zerihan, J., 2000, “Turbulent Wake behind a Single Element Wing in Ground Effect,” Proc. 10th Int. Symp. Appl. Laser Tech. to Fluid Mech.

[14] Zhang, X., and Zerihan, J., 2003, "Off-Surface Aerodynamic Measurements of a Wing in Ground Effect," J. Aircr., **40**(4), pp. 716–725.

[15] Zerihan, J., and Zhang, X., 2001, "A Single Element Wing in Ground Effect; Comparisons of Experiments and Computation," 39th Aerosp. Sci. Meet. Exhib.

[16] Spalart, P. R., and Allmaras, S. R., 1992, "A One-Equation Turbulence Model for Aerodynamic Flows," AIAA Pap. no. 92-0439.

[17] Menter, F. R., 1994, "Two-Equation Eddy-Viscosity Turbulence Models for Engineering Applications," AIAA J., **32**(8), pp. 1598–1605.

[18] Lawson, N. J., Knowles, K., Hart, R. J. E., Wray, J. N.,Eyles, J. M., 2002, "An Experimental Investigation Using PIV of the Underflow of a GA(W)-1 Aerofoil Section in Ground Effect," *Proc. of the 4th MIRA International Vehicle Aerodynamics Conference*, pp. 1–14.

[19] Mahon, S., and Zhang, X., 2005, "Computational Analysis of Pressure and Wake Characteristics of an Aerofoil in Ground Effect," J. Fluids Eng. Trans. ASME, **127**(2), pp. 290–298.

[20] Arrondeau, B., and Rana, Z. ., 2020, "Computational Aerodynamics Analysis of Non-Symmetric Multi-ElementWing in Ground Effect with Humpback Whale Flipper Tubercles," Fluids, **5**(4), p. 247.

[21] Castro, X., and Rana, Z. ., 2020, "Aerodynamic and Structural Design of a 2022 Formula One Front Wing Assembly," Fluids, **5**(4), p. 237.

[22] Yurkovich, R., 2003, "Status of Unsteady Aerodynamic Prediction for Flutter of High Performance Aircraft," J. Aircr., **40**(5), pp. 832–842.

[23] Sangeetha, C., 2015, "Fluid Structure Interaction on AGARD 445.6 Wing at Transonic Speeds," J. Aircr., **2**(4), pp. 28–34.

[24] Chen, X., 2007, "Numerical Simulation of 3D Wing Flutter with Fully Coupled Fluid Structural Interaction," J. Aircr., **36**, pp. 856–867.

[25] Krawczyk, P., Beyene, A., MacPhee, D., 2013, "Fluid Structure Interaction of a Morphed Wind Turbine Blade," Int. J. Energy Res., **37**, pp. 1784–1793.

[26] Bagheri, E., Nejat, A., 2015, "Numerical Aeroelastic Analysis of Wind Turbine NREL

Phase VI Rotor," Energy Equip. Syst., **3**, pp. 45–55.

[27] Wang, L., Quant, R., and Kolios, A., 2016, "Fluid Structure Interaction Modelling of Horizontal-Axis Wind Turbine Blades Based on CFD and FEA," J. Wind Eng. Ind. Aerodyn., **158**, pp. 11–25.

[28] Gaylard, A., Beckett, M., Gargoloff, J., and Duncan, B., 2010, "CFD-Based Modelling of Flow Conditions Capable of Inducing Hood Flutter," SAE Int. J. Passeng. Cars - Mech. Syst., **3**, pp. 675–694.

[29] Ratzel, M. and Dias, W., 2014, "Fluid - Structure Interaction Analysis and Optimization of an Automotive Component," SAE Tech. Pap.

[30] Patil, S., Lietz, R., Woodiga, S., Ahn, H., Larson, L., Gin, R., Elmore, M., and Simpson, A., 2015, "Fluid Structure Interaction Simulations Applied to Automotive Aerodynamics," SAE Tech. Pap., **2015**-**April**(April).

[31] Andreassi, L., Mulone, V., Valentini, P. P., and Vita, L., 2004, "A CFD-FEM Approach to Study Wing Aerodynamics under Deformation," SAE Tech. Pap.

[32] Nazari, A., Chen, L., Battaglia, F., Ferris, J. B., Flintsch, G., Taheri, S., 2020, "Prediction of Hydroplaning Potential Using Fully Coupled Finite Element-Computational Fluid Dynamics Tire Models," ASME. J. Fluids Eng., **142**(10).

[33] Zeng, Y., Yao, Z., Gao, J., Hong, Y., Wang, F., Zhang, F., 2019, "Numerical Investigation of Added Mass and Hydrodynamic Damping on a Blunt Trailing Edge Hydrofoil," ASME. J. Fluids Eng., **141**(8).

[34] Zeng, Y., Yao, Z., Zhang, S., Wang, F., Xiao, R., 2021, "Influence of Tip Clearance On the Hydrodynamic Damping Characteristics of a Hydrofoil," ASME. J. Fluids Eng.

[35] Smith, S. M., Venning, J. A., Giosio, D. R., Brandner, P. A., Pearce, B. W., Young, Y. L., 2019, "Cloud Cavitation Behavior on a Hydrofoil Due to Fluid-Structure Interaction," ASME. J. Fluids Eng., **141**(4).

[36] Dinçer, A. E., Demir, A., Bozkuş, Z., Tijsseling, A. S., 2019, "Fully Coupled Smoothed Particle Hydrodynamics-Finite Element Method Approach for Fluid–Structure Interaction Problems With Large Deflections," ASME. J. Fluids Eng.,

141(8).

[37] Bungartz, H.J., Schäfer, M., Eds., 2006, *Fluid-Structure Interaction: Modelling, Simulation, Optimization*, Springer-Verlag Berlin Heidelberg.

[38] Sigrist, J. F., 2015, *Fluid-Structure Interaction: An Introduction to Finite Element Coupling*, Wiley.

[39] Ryzhakov, P. B., Rossi, R., Idelsohn, S. R. Onate, E., 2010, "A Monolithic Lagrangian Approach for Fluid-Structure Interaction Problems," Comput. Mech., **46**, pp. 883–899.

[40] C. Michler, S.J. Hulshoff, E.H. van Brummelen, R. de Borst, 2004, "A Monolithic Approach to Fluid-Structure Interaction," Comput. Fluids, **33**(5–6), pp. 839–848.

[41] Piperno, S. Farhat, C. Larrouturou, B., 1995, "Partitioned Procedures for the Transient Solution of Coupled Aeroelastic Problems, Part I: Model Problem, Theory and Two-Dimensional Application," Comput. Methods Appl. Mech. Eng., **124**(1–2), pp. 79–112.

[42] Launder, B. E., and Spalding, D. B., 1974, "The Numerical Computation of Turbulent Flows," Comput. Methods Appl. Mech. Eng, **3**, pp. 269–289.

[43] Wilcox, D. C., 1988, "Multiscale Models for Turbulent Flows," AIAA J., **26**(11), pp. 1311–1320.

[44] Yakhot, A., and Orszag, S., 1986, "Renormalisation Group Analysis of Turbulence: I Basic Theory," J. Sci. Comput, **1**(1), pp. 1–51.

[45] Shih, T-H, Liou, W. W, Shabbir, A., Yang, Z., Zhu, J., 1995, "A New k −ε Eddy Viscosity Model for High Reynolds Number Turbulent Flows," Com- put. Fluids, **24**, pp. 227–238.

[46] Roache, P.J., Ghia, K.N., White, F.M., 1986, "Editorial Policy Statement on Control of Numerical Accuracy," J. Fluids Eng. Trans. ASME, **108**, p. 1.

[47] Roache, P. J., 1993, "A Method for Uniform Reporting of Grid Refinement Studies," *Proceedings of Quantification of Uncertainty in Computation Fluid Dynamics*.

[48] Roache, P. J., 1998, *Verification and Validation in Computational Science and*

Engineering, Hermosa Publishers.

[49] Zerihan, J., 2001, “An Investigation on the Aerodynamics of a Symmetrical Airfoil in Ground Effect,” University of Southampton.

[50] FIA, 2018, “2018 Formula One Technical Regulation.”

[51] ANSYS, 2018, “Ansys Composite Library.”

Figure Captions List

Fig. 1 A typical Formula One car with an inverted front wing

Fig. 2 FSI coupling methods (a) one-way (b) two-way

Fig. 3 Workflow of Fluid Structure Interaction system

Fig. 4 A single element wing in ground effect (a) schematic (b) computational grid

Fig. 5 A schematic of computational domain

Fig. 6 Effect of grid sensitivity (a) surface pressure distributions and (b) wake profiles at x/c = 1.2

Fig. 7 Effect of turbulence model variation (a) surface pressure distribution at h/c = 0.224, (b) wake profile at x/c = 1.2 for h/c = 0.224, (c) surface pressure distribution h/c = 0.09, (d) wake profile at x/c = 1.2 for h/c = 0.09

Fig. 8 Chordwise surface pressure distribution at wing centre in ground effect at h/c =0.313 and 0.134 (a) k-ω SST model (b) Realizable k-ε model

Fig. 9 Chordwise surface pressures at wing centre and wing tip in ground effect generated by k-ω SST model (a) h/c=0.313 (b) h/c=0.134

Fig. 10 Spanwise surface pressures in ground effect for different ride heights (a) k-ω SST (b) Realizable k-ε

Fig. 11 Downforce of single element wing in ground effect with various heights

Fig. 12 Drag of single element wing in ground effect with various heights

Fig. 13 u/U velocity contours at heights of h/c = 0.448, 0.224, 0.134, 0.09

Fig. 14 Wake profile at x/c = 1.2 (a) k – ω SST and (b) Realizable k – ε

Fig. 15 Result of deflection and mas stress of single element composite wing with various composite structure

Table Caption List

Table 1	Mechanical properties
Table 2	Summary of GCI study
Table 3	Surface pressure information for various turbulence models, h/c = 0.224
Table 4	Wake information for various turbulence models at x/c = 1.2 for h/c = 0.224
Table 5	Wake information for various ride heights at x/c = 1.2
Table 6	Variation of composite structure for single element wing
Table 7	Results of aerodynamic performance and weights with various composite structure



https://dspace.org/

Aeroelastic analysis of a single element composite wing in ground effect using Fluid Structure Interaction

Bang, Chris Sungkyun; Rana, Zeeshan; Könözsy, László Z.; Rodriguez, Veronica M.; Temple, Clive

2022-04-01
American Society of Mechanical Engineers (ASME)
https://doi.org/10.1115/1.4053089
Bang CS, Rana ZA, Könözsy L, et al., (2022) Aeroelastic analysis of a single element composite wing in ground effect using Fluid Structure Interaction. Journal of Fluids Engineering, Volume 144, Issue 4, April 2022, Paper number FE-21-1108

Downloaded from a DSpace repository. https://dspace.org/